

Cross-calibration of atomic sensors for pressure metrology

Erik Frieling¹, Riley A. Stewart¹, James L. Booth² and Kirk W. Madison¹.

¹*Department of Physics and Astronomy, University of British Columbia, 6224 Agricultural Road, Vancouver, B.C., V6T 1Z1, Canada*

²*Department of Physics, British Columbia Institute of Technology, 3700 Willingdon Avenue, Burnaby, B.C. V5G 3H2, Canada*

(Dated: 27 December 2023)

Atomic sensors have shown great promise for density and pressure metrology in the high, ultra-high, and extremely-high vacuum regimes. Specifically, the density of background gas particles in vacuum can be determined by measuring the collision rate between the particles and an ensemble of sensor atoms. This requires preparing the sensor atoms in a particular quantum state, observing the rate of changes of that state, and using the cross section coefficient for state-changing collisions to convert the rate into a corresponding density. The cross section can be known by various methods including by quantum scattering calculations using an ansatz for the interaction potential between the collision pair, by measurements of the post-collision sensor-atom momentum recoil distribution, or by empirical calibration of the sensor atom at a known density. Identifying systematic errors in the results of these methods can be aided by direct comparisons between them. Alternatively, measurements of different sensor atoms exposed to the same background gas offers another point of comparison free of the systematic errors inherent in creating a background gas at a known density. Here, we present such measurements for two sensor atoms, ⁸⁷Rb and ⁶Li, and a variety of atomic and molecular background gases including H₂, N₂, Ar, Ne, Kr, and Xe. We find results consistent with, yet statistically different at the level of 3.5(5)%, from recent theoretical and experiment measurements. This work demonstrates a model-free method for transferring the primacy of one atomic standard to another sensor atom and highlights the utility of sensor-atom cross-calibration experiments to check the validity of direct measurements and theoretical predictions.

I. INTRODUCTION

Ensembles of cold atoms have been proposed and investigated as a drift-free sensor of absolute pressure and particle flux measurements in vacuum.^{1–16} The background gas density, n , can be determined by measuring the collision rate between the sensor atoms and ambient atoms and molecules via,

$$\Gamma = n \langle \sigma_{\text{tot}} v \rangle. \quad (1)$$

Here knowledge of the thermally averaged total collision cross section ($\langle \sigma_{\text{tot}} v \rangle$) between the sensor atoms and the atoms or molecules in the background gas is essential.

The thermally averaged collision cross sections can be obtained from quantum scattering calculations.^{17–21} However, obtaining potential energy surfaces (PESs), upon which the quantum scattering calculations are based, requires *ab initio* quantum chemistry computations, and sufficient accuracy may be limited to molecular species with a small number of active degrees of freedom. Alternatively, empirical estimates of the total collision cross sections can be obtained from measurements with a background gas of known density.^{22,23} This approach is limited to gas species compatible with the operation of existing orifice flow pressure standards. A third method is to use the sensor atom collision recoil energy (or momentum) distribution to determine the total cross section using the quantum diffractive collision universality law.^{11–13,24} The validity of this latter approach was previously shown for heavy collision partners including Rb+N₂ and Rb+Rb collisions²⁵, but deviations from

the universality law were found for light background collision species.²⁶ The results of these three methods have been found to agree at the level of a few percent with the exception of a few special cases.^{22,23} Understanding the reason for the observed disagreements is essential for determining the true collision cross section.

The main goal of this work is to report the results of a fourth method for validating prior theoretical and experimental work. We perform direct experimental comparisons of the collision rates of two different sensor atom ensembles (containing ⁸⁷Rb or ⁶Li atoms) co-located and exposed to the same background gas species including H₂, N₂, Ne, Ar, Kr and Xe. We also present a comparison of the collision rates when the sensors are exposed to a sample of parahydrogen. The same method presented here was used to compare $\langle \sigma_{\text{tot}} v \rangle_{\text{Rb}+\text{H}_2}$ and $\langle \sigma_{\text{tot}} v \rangle_{\text{Li}+\text{H}_2}$ in a previous study where we measured Γ_{Rb} and Γ_{Li} while the partial pressure of H₂ was varied by heating a non-evaporable getter (NEG)²⁶. This allowed us to determine the ratio of the total cross sections : $R \equiv \langle \sigma_{\text{tot}} v \rangle_{\text{Li}+\text{H}_2} / \langle \sigma_{\text{tot}} v \rangle_{\text{Rb}+\text{H}_2} = 0.83(5)$.

For this new work, we modified our vacuum system by adding a leak valve, allowing us to flow a wide range of background gases. This method of comparing the collision rate coefficients is model-independent and is free of some of the systematic errors inherent with other methods. In particular, the fact that the two sensor atom traps are co-located ensures they are both exposed to the same test gas density, which cannot be guaranteed for measurements comparing a cold atom vacuum standard to a calibrated ion gauge^{12,13} or to a flowmeter and dynamic expansion system where co-location is not

possible.^{22,23} In addition, this co-location measurement provides a systematic-error free method for transferring the primacy of one atomic standard to another sensor atom.

Our results for the ratio of cross sections for various background gases (denoted here by X), $R = \frac{\langle \sigma_{\text{tot}} v \rangle_{\text{Li+X}}}{\langle \sigma_{\text{tot}} v \rangle_{\text{Rb+X}}}$, are generally consistent with prior experimental and theoretical work.^{21–23} However, we do find statistically significant disagreements for certain background species. In prior work, Barker *et al.* report collision-induced loss rates of ^7Li and ^{87}Rb from magnetic traps exposed to test gases whose density was set by a vacuum standard based on a flow meter and a dynamic expansion system.^{22,23} Our findings are consistent with these prior measurements for He, but differ for the heavier species tested (Ne, N_2 , Ar, Kr, and Xe). Klos and Tiesinga report cross sections found from quantum scattering calculations.²¹ Our findings are consistent with these calculations for two of the lightest species tested, H_2 and Ne, but appear to indicate that the calculations may have systematically underestimated R by approximately 3.5% for He, N_2 , Ar, Kr, and Xe. We believe this work indicates the need for further refinement of the different methods of determining $\langle \sigma_{\text{tot}} v \rangle$.

II. EXPERIMENTAL PROCEDURE

In this work, the ratio $R = \frac{\langle \sigma_{\text{tot}} v \rangle_{\text{Li+X}}}{\langle \sigma_{\text{tot}} v \rangle_{\text{Rb+X}}}$ is measured directly by confining Rb and Li atoms to the same spatial region where they are exposed to the same background gas density. The R value for a test species, X, is then obtained by comparing the sensor atom collision rate sensitivities to density changes of that test gas. An exact knowledge of the test gas density or the residual background density is not required, as long as only the test gas density is changed. This method is in contrast to prior experimental work that relied on another pressure standard to set a known pressure^{22,23}.

For a trap of sufficiently small depth that every collision with species X liberates a sensor atom from the trap, we can write,

$$\Gamma_{\text{Rb}}(n_{\text{X}}) = n_{\text{X}} \langle \sigma_{\text{tot}} v \rangle_{\text{Rb+X}} + \Gamma_{(\text{Rb},0)} \quad (2)$$

$$\Gamma_{\text{Li}}(n_{\text{X}}) = n_{\text{X}} \langle \sigma_{\text{tot}} v \rangle_{\text{Li+X}} + \Gamma_{(\text{Li},0)} \quad (3)$$

where $\Gamma_{(\text{Rb},0)}$ and $\Gamma_{(\text{Li},0)}$ are the baseline loss rates of Rb and Li measured before the density of species X is changed by flowing it into the vacuum.

At each value of n_{X} (representing the change in the density of species X), measurements of $\Gamma_{\text{Rb}}(n_{\text{X}})$ and $\Gamma_{\text{Li}}(n_{\text{X}})$ are made in pairs with minimum time between the two measurements so that the value of n_{X} is the same for each data pair. From these measurements, R can be determined as,

$$R \equiv \frac{\langle \sigma_{\text{tot}} v \rangle_{\text{Li+X}}}{\langle \sigma_{\text{tot}} v \rangle_{\text{Rb+X}}} = \frac{\Gamma_{\text{Li}}(n_{\text{X}}) - \Gamma_{(\text{Li},0)}}{\Gamma_{\text{Rb}}(n_{\text{X}}) - \Gamma_{(\text{Rb},0)}}. \quad (4)$$

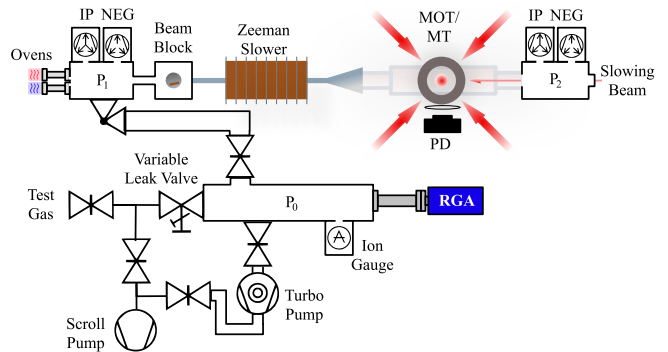


FIG. 1. Schematic of the experimental apparatus. The test gas is introduced into the vacuum system through a variable leak valve, resulting in a pressure P_0 in the first chamber set by the leak rate of the valve and the pumping rate of the turbo molecular pump. To ensure the gas purity, a small reservoir behind the leak valve is filled with the test gas at a pressure of approximately 10^5 Pa after being evacuated using the scroll pump. A residual gas analyzer (RGA) is used to characterize the background gas constituents of P_0 and to verify that the leaked gas is free of contaminants. The gas flows through a 1.5 m long bellows into the oven chamber, which contains the Li and Rb ovens, a non-evaporable getter (NEG) and an ion pump (IP), reaching a pressure P_1 . The atomic beams coming from the neighboring Li ($T = 400$ °C) and Rb ($T = 100$ °C) ovens are decelerated using a Zeeman slower and captured in a magneto-optic trap (MOT). The atoms are subsequently transferred to a magnetic trap (MT) in which they suffer collision-induced losses from the background gas, now at P_2 due to differential pumping. The beam block can be rotated to block the directed atomic flux from the ovens during the measurement. It is located next to a cold finger kept at 5 °C that collects some of the excess Rb atoms to avoid contamination of the vacuum system. The atoms remaining in the MT after exposure are recaptured in the MOT, and their fluorescence is measured using a photodiode (PD).

From Eq. 4 one observes that a plot of the $\Gamma_{\text{Li}}(n_{\text{X}})$ versus $\Gamma_{\text{Rb}}(n_{\text{X}})$ pairs measured at each background gas density will yield a straight line with a slope of R .

The apparatus used to perform these loss rate measurements of both Rb and Li atoms exposed to the same background gas is very similar to one described in previous work, although the current iteration is a complete rebuild.^{26,27} A separate vacuum chamber with a variable leak valve, ion gauge and residual gas analyzer (RGA) were connected near the oven section of our apparatus. This allows us to control the partial pressure of a background gas introduced through the leak valve.

A schematic of the apparatus is shown in Fig. 1. When introducing a new gas, we start by evacuating a small reservoir connected to the variable leak valve and the scroll pump. Subsequently, we fill the reservoir with the test gas at a pressure of approximately 10^5 Pa, and seal it. We then vary the pressure of the background gas in the magnetic trap chamber, in the range from 10^{-8} to 10^{-7} Pa, by changing the small leak rate using the

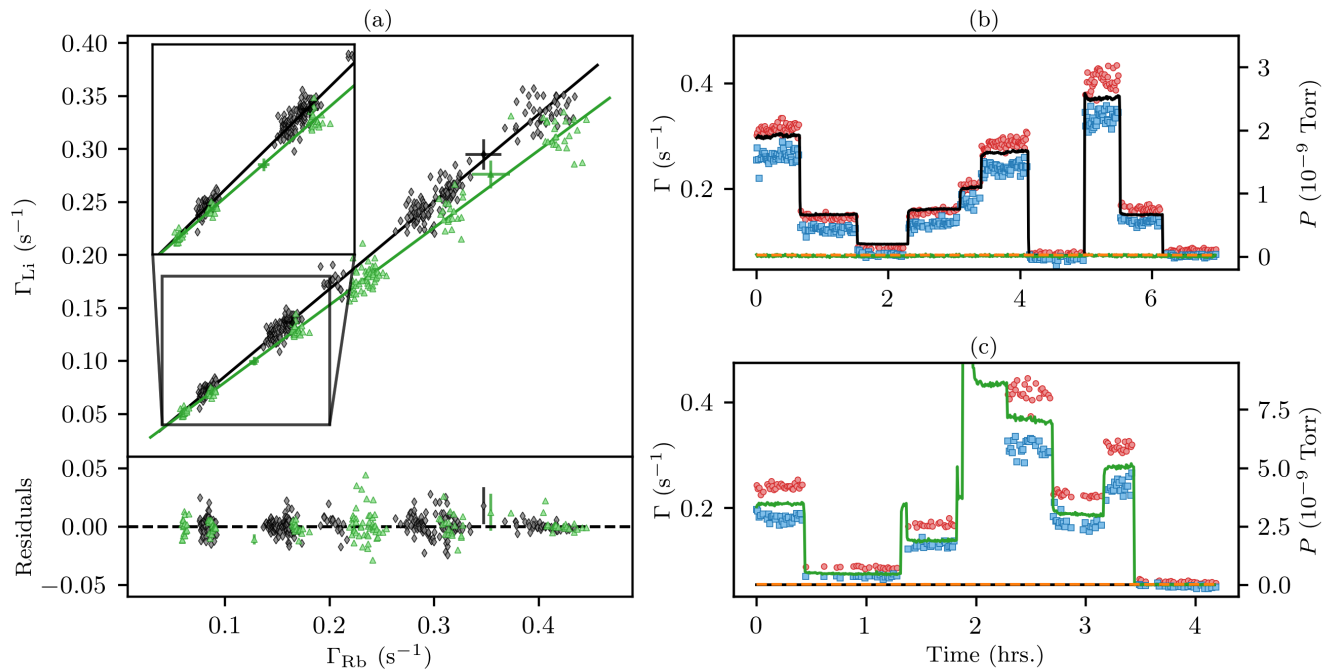


FIG. 2. (a) Magnetic trap loss rates for ${}^6\text{Li}$ and ${}^{87}\text{Rb}$ atoms, plotted as the ordered pair $(\Gamma_{\text{Rb}}, \Gamma_{\text{Li}})$, when exposed to H_2 (black diamonds) and He (green triangles) gas. The measurements are fit to lines (same color as markers) whose slope provides the ratio of the loss rates and thus the ratio of the cross sections. We find $R = \frac{\Gamma_{\text{Li}}}{\Gamma_{\text{Rb}}} = \frac{\langle \sigma_{\text{tot}} v \rangle_{\text{Li}+\text{X}}}{\langle \sigma_{\text{tot}} v \rangle_{\text{Rb}+\text{X}}} = 0.824 \pm 0.005$ (0.729 ± 0.006) for H_2 (He). These R values are derived from the raw measurements $R^{\text{meas}} = 0.825(5)$ ($0.729(6)$) corrected for finite trap depth effects as explained in appendix section A 1. Example error bars are shown for a few samples with the rest suppressed for readability. Results for all background gases tested are summarized in table I. (b) and (c) show the loss rate measurements for Li (blue squares) and Rb (red circles) from the shallow magnetic trap together with the partial pressure of H_2 (black), He (green) and N_2 (orange dashed) as measured by a residual gas analyzer (RGA) and scaled using an appropriate calibration factor to match the pressure at the location of the atoms (see Appendix A 5).

variable leak valve. The RGA is used to verify the leaked gas is free of contaminants.

The oven section and magnetic trap section, where the trap loss measurements are performed, are connected by a 12 mm long, 6 mm diameter differential pumping tube with an estimated Hydrogen conductance of 0.85L/s^{28} , so the partial pressure read by the RGA and ion pump is substantially larger than what is experienced by the trapped atoms. We turn off the ion pump in the oven section to prevent sputtering and pressure fluctuations due to Argon instability when pumping heavy noble gases.²⁹ The much lower pressure in the magnetic trap section eliminates the need to do the same for the ion pump located there. Instead, we leave this second ion pump on, because it lowers the baseline pressure achieved when not flowing the test gas, and this enhances the experimental precision achieved in R . In addition, we verified that turning off this ion pump does not affect the measurements.

For both species, co-located magneto-optic traps (MOTs) capture atoms from thermal, parallel atomic beams that are decelerated and cooled by a Zeeman slower.²⁷ To ensure a similar number of atoms are loaded

for each experimental shot, the Zeeman slowing light is extinguished when the fluorescence from the MOT reaches a set value V_{MOT} . The atoms are then optically pumped to the desired hyperfine state and all light is extinguished, at which point they are confined by the quadrupole magnetic field. We then ramp the magnetic field gradient in 20 ms to the hold gradient used for the MT phase. After a variable hold time in the MT, the atoms are recaptured in the MOT and their fluorescence $V_{\text{MT}}(t)$ is recorded using a photodiode. To improve the signal to noise, we determine the recaptured fraction $f_{\text{recap}}(t) = V_{\text{MT}}(t)/V_{\text{MOT}}$ as described previously.²⁶ This quantity is insensitive to the residual variations in the number of atoms loaded into the MOT.

Glancing collisions which do not induce trap loss can lead to heating of the ensemble and, consequently, influence the measured loss rate in a non-trivial way (see appendix A 1). To minimize this effect, the Li and Rb atoms are confined in a very shallow magnetic trap for these measurements. The Rb atoms are confined with an axial magnetic field gradient of $b' = 35\text{ G/cm}$, and the trap depth is limited to $U_{\text{Rb}}/k_B = 125\ \mu\text{K}$ by applying radio-frequency (RF) radiation repeatedly sweeping

between 20 MHz and 40 MHz for 2s at the end of the variable hold time. We verified that sweeping the RF from 0 to 40 MHz completely empties the trap. The RF induces spatially localized transitions between the trapped, weak-field seeking $|F = 1, m_F = -1\rangle$ and the untrapped $|F = 1, m_F = 0\rangle$ and anti-trapped, strong-field seeking $|F = 1, m_F = 1\rangle$ magnetic Zeeman states. More details are provided in the appendix A 1. For ${}^6\text{Li}$, the atoms are confined in an axial gradient $b' = 100$ G/cm. We do not apply any RF for ${}^6\text{Li}$, since the field dependence of the magnetic moment of the $|F = 1/2, m_F = -1/2\rangle$ state limits the trap depth to $U_{\text{max}}/k_B = 294$ μK .²⁶

Because the optimal Zeeman+MOT loading and MT trapping parameters are so different for the two sensor atoms, we alternate between loss rate measurements instead of making a simultaneous measurements of a MT loaded with both sensor atoms. Since we require that n_X be the same for each sensor atom loss rate measurement, we perform measurements at a series of different but constant leak rates. To mitigate the effect of any slow drift of the background gas density, we minimize the time between sensor atom measurements by performing two-point measurements, alternating between trapped species. We measure the recapture fraction at $t = 0$ and at $t = t_1$, and we compute the loss rate as $\Gamma = \ln[f_{\text{recap}}(t = t_1)/f_{\text{recap}}(t = 0)]/t_1$. We interlace the measurements for the two species such that the two-point lifetime measurement for the two species is overlapped in time. Thus a single $(\Gamma_{\text{Rb}}, \Gamma_{\text{Li}})$ point is collected as follows:

1. Measure $f_{\text{recap}}(t = 0)$ for Li
2. Measure $f_{\text{recap}}(t = 0)$ for Rb
3. Measure $f_{\text{recap}}(t = t_1)$ for Li
4. Measure $f_{\text{recap}}(t = t_1)$ for Rb

To optimize the sampling, we choose a hold time for each species such that $t_1 \equiv 1.5/\bar{\Gamma}$, where $\bar{\Gamma}$ is an estimate of the Rb or Li loss rate that is updated based on the average of the previous five measurements. In addition, the order in which the $t = 0$ and $t = t_1$ measurements are taken is randomized to mitigate the effect of systematic drifts of the MOT to MT transfer efficiency. We also observed that the decay of the recapture fraction, even at the very lowest background pressures where non-linearities in the decay would be most apparent, is purely exponential (i.e. $f_{\text{recap}}(t) = f_{\text{recap}}(0)e^{-\gamma t}$). The consequence is that a two-point measurement is sufficient to determine the total loss rate at any test gas pressure.

Finally, we note that for this study, we use ${}^6\text{Li}$ instead of ${}^7\text{Li}$ sensor atoms. Because the ${}^6\text{Li}$ atom is a composite Fermion, when we prepare and magnetically trap a spin polarized sample in the $|F = 1/2, m_F = -1/2\rangle$ state at a temperature below 300 μK , intra-trap collisions do not occur. This is because, s-wave collisions are forbidden due to the Pauli principle and p-wave collisions are frozen out at this temperature.

III. DISCUSSION OF RESULTS

In Fig. 2 we plot the ordered pairs $(\Gamma_{\text{Rb}}, \Gamma_{\text{Li}})$ for different values of the H_2 and He densities in a 2D scatter plot where the abscissa is the Rb loss rate and the ordinate is the Li loss rate. The measurements for H_2 and He were chosen as examples, because they represent the highest and lowest values of R respectively. We fit these points to a linear model using orthogonal distance regression (ODR) and extract the slope R . The individual points are weighted by the statistical uncertainty, which we estimate by characterizing the variation in f_{recap} at constant pressure and using uncertainty propagation to find the uncertainty in Γ . In Fig. 2 these uncertainties are suppressed for visual clarity, except for a few selected points.

Figs. 2b and 2c show the same data as a time series, together with the partial pressures measured by the RGA. For each gas under test, the partial pressure was increased and decreased several times during each experimental run to minimize the effects of any systematic, slow variation in the background pressure on the measurement. We also repeated each measurement on three different days and observed the same values for R to within 1%.

To compare the current results with previous work, we must compensate the measured loss rates for the finite trap depth, U , at which the measurements were carried out. Namely, the quantity that we measure,

$$R^{\text{meas}} = \frac{\langle \sigma_{\text{loss}} v \rangle_{\text{Li+X}}}{\langle \sigma_{\text{loss}} v \rangle_{\text{Rb+X}}} \quad (5)$$

becomes R in the limit $U \rightarrow 0$. Kłos and Tiesinga (KT)²¹ report a convenient quadratic description for extrapolating $\langle \sigma_{\text{tot}} v \rangle$ from the measured $\langle \sigma_{\text{loss}} v \rangle(U)$ (labelled K and L , respectively, in their work) for shallow traps,

$$\langle \sigma_{\text{loss}} v \rangle = \langle \sigma_{\text{tot}} v \rangle - a_{\text{gl}}U + b_{\text{gl}}U^2. \quad (6)$$

Using the KT a_{gl} and b_{gl} coefficients, we determine R . (See Appendix A 1 and Table IV.) Since we use such shallow magnetic traps to confine the sensor atoms, the trap depth correction for the Li-X measurements is less than 0.1%, and the Rb-X correction is less than 0.5% for all collision partners. A similar trap depth correction is applied to the Li-X loss rate coefficients measured by Barker *et al* (BExp)^{22,23}.

The data presented here were collected at a room temperature of 298(2)K. By contrast Barker *et al* (BExp)^{22,23} measured the Li-X loss rate coefficients at 300.2(2.9)K and the Rb-X loss rate coefficients at 295.2(3)K. Therefore, the BExp results were temperature corrected to $T = 298$ K following the prescription of Kłos and Tiesinga (KT)²¹. Namely,

$$\langle \sigma_{\text{tot}} v \rangle = K_0 + K_1 \cdot (T - 300 \text{ K}) \quad (7)$$

where K_0 is the loss rate coefficient at $T = 300$ K, and K_1 is the linear temperature correction coefficient. Thus,

TABLE I. The measured cross section ratios, $R_{6,87}^{\text{meas}} = \langle \sigma_{\text{loss}} v \rangle_{\text{Li+X}} / \langle \sigma_{\text{loss}} v \rangle_{\text{Rb+X}}$, and the trap-depth-corrected ratios $R_{6,87} = \langle \sigma_{\text{tot}} v \rangle_{6\text{Li+X}} / \langle \sigma_{\text{tot}} v \rangle_{87\text{Rb+X}}$ in this work. $R_{7,87}^{\text{KT}}$ are calculated from quantum scattering calculations²¹ of $\langle \sigma_{\text{tot}} v \rangle_{7\text{Li+X}}$ and $\langle \sigma_{\text{tot}} v \rangle_{87\text{Rb+X}}$. $R_{7,87}^{\text{BExp}}$ are computed from previous measurements²³ of $\langle \sigma_{\text{tot}} v \rangle_{7\text{Li+X}}$ and $\langle \sigma_{\text{tot}} v \rangle_{87\text{Rb+X}}$. $R_{6,87}^{\text{SExp}}$ is the value from our prior direct cross-species measurement²⁶ and $R_{6,87}^{\text{th}}$ is the quantum scattering computation reported in the same paper. The final column shows the values for $R_{6,87}^{\text{C6}}$ predicted by Eq. 10. Agreement with prior theory, $R_{7,87}^{\text{KT}}$, is found for X=H₂ and Ne; however, statistically significant deviations both from previous theory and experiment are found for other species. All of the R values listed here have been adjusted for a room temperature of 298K, as described in the text. These results are also plotted in Fig. 3. The statistical uncertainties (type A) are listed in brackets beside each entry. The systematic uncertainties (type B), as discussed in Appendix A, are much lower and their maximum values are listed in Table II.

| Species | (This work) | | $R_{7,87}^{\text{KT}}$ (21) | $R_{7,87}^{\text{BExp}}$ (22,23) | $R_{6,87}^{\text{SExp}}$ (26) | $R_{6,87}^{\text{(th.)}}$ (26) | $R_{6,87}^{\text{C6}}$ |
|-----------------|--------------------------|------------|-----------------------------|----------------------------------|-------------------------------|--------------------------------|------------------------|
| | $R_{6,87}^{\text{meas}}$ | $R_{6,87}$ | | | | | |
| pH ₂ | 0.828(6) | 0.827(6) | 0.82(3) | | | 0.869 | 0.801(3) |
| H ₂ | 0.825(5) | 0.824(5) | 0.82(3) | | 0.83(5) | 0.869 | 0.801(3) |
| He | 0.729(6) | 0.729(6) | 0.69(2) | 0.73(2) | | | 0.775(1) |
| Ne | 0.798(5) | 0.797(5) | 0.78(11) | 0.74(2) | | | 0.778(2) |
| N ₂ | 0.798(5) | 0.796(4) | 0.76(2) | 0.75(3) | | | 0.789(1) |
| Ar | 0.798(5) | 0.796(5) | 0.768(4) | 0.721(13) | | | 0.788(1) |
| Kr | 0.798(5) | 0.795(5) | 0.769(4) | 0.78(2) | | | 0.797(2) |
| Xe | 0.803(4) | 0.799(4) | 0.779(8) | 0.77(2) | | | 0.803(2) |

using the measured loss rate coefficients reported in²³, K^{BExp} , and the K_1 reported by KT²¹ for each collision partner pair, A-X we have,

$$K_{A,X}^{\text{BExp}}(298\text{K}) = K_{A,X}^{\text{BExp}}(T_{\text{exp}}) + K_{1,(A,X)} \cdot (298\text{K} - T_{\text{exp}}) \quad (8)$$

where T_{exp} is the ambient temperature of the experimental result. The theoretical coefficients, $K_{A,X}^{\text{KT}}(298\text{K})$ were computed from Eq. 7. This allowed us to compute R values that can be compared to our present data directly. In the following discussion the room temperature value, $T = 298\text{K}$, will be omitted.

The results of our measurements are summarized in Tab.I and Fig. 3, where they are compared to recent theoretical and experimental results^{21-23,26}. We note that our measurements utilize ⁶Li and ⁸⁷Rb atoms and thus we report $R_{6,87} \equiv \frac{\langle \sigma_{\text{tot}} v \rangle_{6\text{Li+X}}}{\langle \sigma_{\text{tot}} v \rangle_{87\text{Rb+X}}}$, whereas prior theoretical and experimental results are for ⁷Li and ⁸⁷Rb atoms and thus provide $R_{7,87} \equiv \frac{\langle \sigma_{\text{tot}} v \rangle_{7\text{Li+X}}}{\langle \sigma_{\text{tot}} v \rangle_{87\text{Rb+X}}}$.

The data set is observed to separate into two groups: the higher mass collision partners for which the ratio is almost constant ($R_{6,87} \simeq 0.8$ for N₂, Ne, Ar, Kr, and Xe), and the lower mass collision partners, H₂, He, for which R is distinct from this constant value.

The $R_{6,87}$ values reported here for H₂ and Ne are consistent with the quantum scattering calculations (QSC) of Klos and Tiesinga²¹ (KT). Specifically, the measured value for H₂, $R_{6,87} = 0.824(5)$, agrees with the KT QSC value, $R_{7,87}^{\text{KT}} = 0.82(3)$. It is also in agreement with our previous measurement, $R_{6,87}^{\text{SExp}} = 0.83(5)$. Our earlier experimental measurement also employed co-located sensor ensembles, but relied on a different source for the H₂ gas (the H₂ outgassing induced by heating a non-evaporable getter pump). The measured value for He, $R_{6,87} = 0.729(6)$, agrees with the updated BExp

value^{22,23}, $R_{7,87}^{\text{BExp}} = 0.73(2)$, and is within 2 standard deviations of the KT QSC value, $R_{7,87}^{\text{KT}} = 0.69(2)$. Finally, the value for Ne, $R_{6,87} = 0.797(5)$ is in agreement with the KT QSC value, $R_{7,87}^{\text{KT}} = 0.78(11)$ and but is outside 2 standard deviations of the BExp measurement of $R_{7,87}^{\text{BExp}} = 0.74(2)$. By contrast, the $R_{6,87}$ values for the heavier species (N₂, Ar, Kr, and Xe) are systematically larger than either the KT QSC or the BExp experimental values (see Tab. I). We discuss these discrepancies and potential causes here and in the appendix.

A unique advantage of our experimental technique and the data we have obtained is that the Li and Rb sensor atoms are exposed to exactly the same background pressure, since the traps are co-located. In the experimental work of Barker *et al*^{22,23}, $\langle \sigma_{\text{tot}} v \rangle$ was deduced from measurements of the loss rate at background gas densities, n , created by an orifice flow standard. We hypothesize that pressure gradients may have existed between the orifice flow standard output and the locations of the two separate CAVS sensor assemblies connected to the standard. Indeed, the ambient temperatures reported for these two sensor ensembles were different, indicating variations in the local test environments. Such gradients could result in a systematic error in the inferred pressure and thus the $\langle \sigma_{\text{tot}} v \rangle$ values reported. As the lightest noble gas, He has the highest conductance through the vacuum system and does not exhibit significant out-gassing or surface adsorption, so pressure gradients are expected to be smallest for this species. This may account for the close agreement between the experimental values. By contrast, we observe larger discrepancies between the $R_{7,87}^{\text{BExp}}$ and the $R_{6,87}$ values reported here for the heavier species (see Tab. I), consistent with this hypothesis.

A remarkable feature is the almost identical $R_{6,87}$ values for the highest mass collision partners, N₂, Ar, Kr, and Xe. This same trend is seen in the quantum scattering computed values, $R_{7,87}^{\text{KT}}$, albeit with a different av-

erage value. We believe that this collision partner independence of $R_{6,87}$ is related to universal nature of the collisions^{11–13,25}. For these heavy collision partners, both the loss rate variation with trap depth and the total cross section are expected to be independent of the interaction potential at short range. In this case, the $\langle\sigma_{\text{tot}}v\rangle$ values are principally determined by the long-range van der Waals interactions (characterized by the dominant term, $-C_6/r^6$, where r is the inter-species separation). For the purposes of this discussion, write the cross section as

$$\langle\sigma_{\text{tot}}v\rangle = \langle\sigma_{\text{tot}}v\rangle_{C_6} + \langle\sigma_{\text{tot}}v\rangle_{\text{corr}} \quad (9)$$

where $\langle\sigma_{\text{tot}}v\rangle_{C_6}$ is the prediction based on the Jeffreys-Born approximation,¹¹

$$\langle\sigma_{\text{tot}}v\rangle_{C_6} = 8.49464 \left(\frac{C_6}{\hbar v_p}\right)^{\frac{2}{5}} v_p + 7.19729 \left(\frac{\hbar}{\mu}\right) \left(\frac{C_6}{\hbar v_p}\right)^{\frac{1}{5}}. \quad (10)$$

Here v_p is the peak velocity of the Maxwell-Boltzmann distribution of the background species, and μ is the reduced mass of the colliding partners. The $\langle\sigma_{\text{tot}}v\rangle_{\text{corr}}$ are the corrections introduced by the other long-range van der Waals interactions and the details of the core repulsion. We note that because these corrections affect the quantum-mechanical scattering amplitude, the value of $\langle\sigma_{\text{tot}}v\rangle_{\text{corr}}$ can be either positive or negative, corresponding to a constructive or destructive interference to the total cross section. Using this, we can write,

$$R = R_{C_6} \cdot \left[\frac{(1 + T_{\text{corr},C_6})_{\text{Li-X}}}{(1 + T_{\text{corr},C_6})_{\text{Rb-X}}} \right] \quad (11)$$

where

$$R_{C_6} = \frac{\langle\sigma_{\text{tot}}v\rangle_{C_6}^{\text{Li-X}}}{\langle\sigma_{\text{tot}}v\rangle_{C_6}^{\text{Rb-X}}} \quad (12)$$

and

$$T_{\text{corr},C_6} = \frac{\langle\sigma_{\text{tot}}v\rangle_{\text{corr}}}{\langle\sigma_{\text{tot}}v\rangle_{C_6}}. \quad (13)$$

The final column in Table I shows the $R_{6,87}^{C_6}$ predictions using the C_6 values taken from Jiang *et al.*³⁰ Computing the average of our measured values for the heaviest species (N_2 , Ar, Kr, and Xe) yields

$$\langle R_{6,87} \rangle = 0.7965(9), \quad (14)$$

and appears to agree with the corresponding average value for the $R_{6,87}^{C_6}$ predictions,

$$\langle R_{6,87}^{C_6} \rangle = 0.795(5). \quad (15)$$

This result implies that the ratio of the correction terms in Eq. 11 cancel and that R_{C_6} is a good approximation for any two alkali sensor atoms. Thus, one can

use the predicted $R_{A,B}^{C_6}$ value and a measurement of $\langle\sigma_{\text{tot}}v\rangle$ for one sensor atom collision-partner pair (A-X) to deduce the $\langle\sigma_{\text{tot}}v\rangle$ corresponding to a different sensor atom (B-X). We note that for ${}^7\text{Li}:\text{Rb}$, the average is $\langle R_{7,87}^{C_6} \rangle = 0.792(5)$ owing to the μ dependence of the second term of Eq. 10.

We also had the opportunity to measure $R_{6,87}$ for >99.9% pure para-hydrogen ($p\text{H}_2$) created using a closed cycle He fridge and a (FeOH)O magnetic converter at 14 K.³¹ This gas was produced and provided to us by the group of Professor Takamasa Momose of the University of British Columbia. We found no statistical difference in the value of R for para-hydrogen compared to normal hydrogen, as shown in Table I. Normal hydrogen is a mixture of ortho- and para-hydrogen with nuclear spins, $I = 1$ and 0, respectively. In the $X\ ^1\Sigma_g^+$ ground molecular state, the wavefunction symmetry demands that $I + J$ is even, where J is the rotational quantum number of the rovibronic state. Thus, ortho-hydrogen populates only the odd J rotational levels and para-hydrogen populates only the even rotational levels. To convert from ortho- H_2 to para- H_2 , or vice-versa, the nuclei must experience a magnetic dipole gradient to flip the nuclear spin. As we are measuring long-range collisions, these gradients are negligible. In addition, for these glancing collisions there is insufficient energy exchanged to result in the change in rotational state required for a change in nuclear spin of the molecule. Thus we expected the $R_{6,87}$ (and $\langle\sigma_{\text{tot}}v\rangle_{\text{Li+X}}$, $\langle\sigma_{\text{tot}}v\rangle_{\text{Rb+X}}$) to be the same for H_2 and $p\text{H}_2$, as our measurements confirm.

In the appendices, we discuss the systematic errors associated with the $R_{6,87}$ values reported here. These are summarized in Table II. The largest systematic error (type B error) is associated with the corrections due to the finite trap depth confining the sensor atoms deviating the measured value of $\Gamma_{\text{loss}} = n\langle\sigma_{\text{loss}}v\rangle$ from the target $\Gamma = n\langle\sigma_{\text{tot}}v\rangle$. This systematic error has been removed from our quoted values of $R_{6,87}$ in Tab. I, and it is well below the 1% level for all collision partners for the trap depths employed in this study. Thus, we are confident that the discrepancies we observe indicate the need for the refinement of both theoretical and experimental determinations of $\langle\sigma_{\text{tot}}v\rangle$.

In Appendix B, we speculate on what these discrepancies may be telling us regarding the theoretical description of the interaction potentials used by Klos *et al.* In particular, we discuss the size of the contributions of the core potential to the $\langle\sigma_{\text{tot}}v\rangle$ values, which is much more significant for collisions with Li sensor atoms than for Rb. We provide a few examples of how physically reasonable changes of the shape and details of the core potential can lead to changes of $\langle\sigma_{\text{tot}}v\rangle$ on the few percent level for collisions with Li sensor atoms.

The hypothesis that the potentials used to compute the Li-X cross sections may need refinement is supported both by our experimental results and by the experimental values of $\langle\sigma_{\text{tot}}v\rangle$ for ${}^7\text{Li}$ collisions with the heavier collision partners reported by Barker *et al.*²². The ma-

TABLE II. Summary of the systematic error estimates (type B errors) associated with this work. The largest systematic errors arise from the finite trap depth of the confined sensor atoms shifting the $\Gamma_{\text{loss}}^{\text{meas}}$ away from Γ_{tot} . This uncertainty has been removed from the $R_{6,87}$ values quoted in Table I. Detailed discussions of each uncertainty can be found in the Appendices.

| Error Source | Estimate, $\frac{\delta R}{R}$ |
|---|--------------------------------|
| $\Gamma_{\text{Loss}}^{\text{meas}}$ deviation from Γ_{tot} | < 0.5% |
| Ensemble Heating Induced Error | < 0.004% |
| 2-Body Intra-Trap Loss Uncertainty | < 0.05% |
| Ambient Temperature Uncertainty | < 0.012% |
| Baseline Gas Composition Variation | < 0.14% |

majority of the experimental values reported by Barker *et al.* are systematically 2-4% higher than the theoretical predictions. The results presented here, with their attendant high precision, offer an exciting opportunity to examine the shape of the core repulsion for Li collisions experimentally.

IV. CONCLUSIONS

The collision-induced loss rate of cold, trapped atoms from a shallow trap due to a background gas, X, can be written as, $\Gamma = n_X \langle \sigma_{\text{loss}} v \rangle$, where n_X is the density of the gas, and $\langle \sigma_{\text{loss}} v \rangle$ is the total collision loss rate coefficient characterizing the collision interaction. A knowledge of the total collision loss rate coefficient allows the measured loss rate to be used to measure the gas density directly. Here we have measured the loss rates of ^{87}Rb atoms and of ^7Li atoms from shallow magnetic traps for H_2 , He, Ne, N_2 , Ar, Kr, and Xe gases introduced into the vacuum system. The loss rates were recorded in pairs, $(\Gamma_{\text{Rb-X}}, \Gamma_{\text{Li-X}})$, at a series of gas densities, n_X , for each gas species, X. These loss rates, measured at exceedingly low trap depths, were used to compute the collision rate coefficient ratio, $R = \langle \sigma_{\text{tot}} v \rangle_{\text{Li-X}} / \langle \sigma_{\text{tot}} v \rangle_{\text{Rb-X}}$. The innovation and advantages of this method are (i) the cold trapped ensembles are co-located in the vacuum system ensuring that the two trapped ensembles experience the same background gas densities free from any systematic errors that may be encountered for ensembles probing the vacuum at different locations, and (ii) the ratiometric method means that the density of the test gas need not be measured or known to obtain R . The only requirement is that the test gas density remain constant over the measurement duration (tens of seconds). This method provides an experimental technique for transferring the known or calibrated loss rate coefficient for one species pair (A-X) to a second species pair (B-X), where X is the background gas and A and B are two different trapped sensor atom ensembles. This experimentally determined loss rate ratio, R , also provides systematic-error

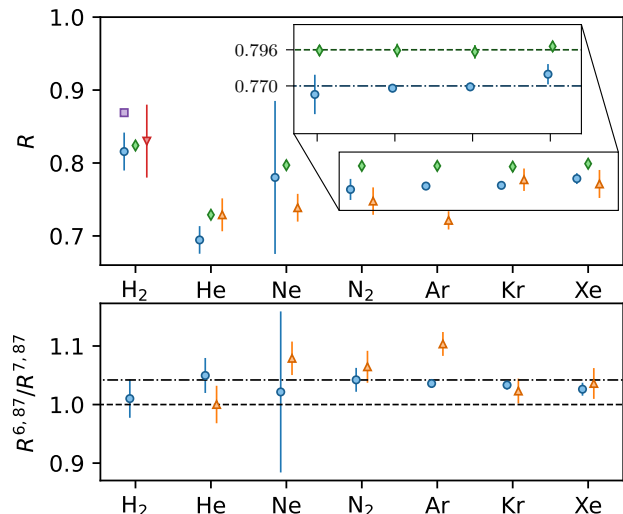


FIG. 3. Top panel: $R_{6,87} = \frac{\Gamma_{\text{Li}}}{\Gamma_{\text{Rb}}} = \frac{\langle \sigma_{\text{tot}} v \rangle_{\text{Li+X}}}{\langle \sigma_{\text{tot}} v \rangle_{\text{Rb+X}}}$ as measured in this work (green diamonds) for variety of background gases, compared to $R_{7,87}^{\text{BExp}}$ (23) (orange triangles) and quantum scattering calculations values, $R_{7,87}^{\text{KT}}$ (21) (blue circles). Our previous experimental result (red nabla) and theoretical prediction (purple square) for H_2 are also included. 26 These data are summarized in Table I.

The inset shows the $R_{6,87}$ data and the $R_{7,87}^{\text{KT}}$ values for N_2 , Ar, Kr, and Xe. The dashed lines are the average values, $\langle R \rangle$ for these collision partners. Note that the $R_{6,87}$ and $R_{7,87}^{\text{KT}}$ are remarkably constant for the heavier collision partners.

Bottom panel: Ratio of $R_{6,87}$ determined using our cross-species calibration method (this work) to KT theory 21 (blue circles) and the ratio of $R_{6,87}$ to Bexp measurements 23 (orange triangles) for the different collision partners. The dashed line corresponds to a value of 1.00 (perfect agreement). The dot-dashed line is the average, $\langle R_{6,87}/R_{7,87}^{\text{KT}} \rangle = 1.035(5)$ for $X = \text{N}_2, \text{Ar}, \text{Kr}, \text{and Xe}$.

free measurements that can be directly compared to *ab initio* computations of the loss rate coefficients $\langle \sigma_{\text{tot}} v \rangle$. We believe these measurements can be used to guide refinements of the theoretical potential energy surfaces describing the collision interactions.

The measurements indicate that the cross section ratios are the same for the heaviest species tested ($X = \text{N}_2, \text{Ar}, \text{Kr}, \text{and Xe}$) with an average of $\langle R_{6,87} \rangle = 0.7965(9)$. This is remarkably close to the purely C_6 prediction $\langle R_{6,87}^{\text{C}_6} \rangle = 0.795(5)$ for $^6\text{Li-X:}^{87}\text{Rb-X}$. This finding appears to be consistent with the universality hypothesis that asserts that the total cross section for heavy collision partners is principally determined by the long-range van der Waals interactions 11 . By contrast the Klos and Tiesinga (KT) quantum scattering computation ratio predicts $\langle R_{7,87}^{\text{KT}} \rangle = 0.770(3)$ and the BExp measurements yield $\langle R_{7,87}^{\text{BExp}} \rangle = 0.756(21)$ for these species. The possible experimental sources of systematic error in our measurements have been examined in this paper, and we do not believe that they are large enough to explain

these discrepancies. In particular, we find that the deviation of the measured Γ_{loss} from the true Γ_{tot} due to the finite shallow trap depth and cold atom ensemble energy distributions is $< 0.5\%$, ensemble collision-induced heating uncertainties are less than 0.004% , unaccounted 2- and 3-body intra-trap collisions $< 0.05\%$, uncertainty associated with variation of the ambient temperature of the test environment $< 0.012\%$, and drift of the baseline pressure $< 0.14\%$.

Because of our systematic errors are so small and because the majority of the experimental values of $\langle \sigma_{\text{tot}} v \rangle$ for ${}^7\text{Li}$ collisions with test gases reported by Barker *et al.*²² are systematically 2-4% higher than the theoretical predictions, we hypothesize that the observed systematic differences in our $R_{6,87}$ values compared to the $R_{7,87}^{\text{KT}}$ may arise from errors in the potential energy surfaces used in the KT quantum scattering computations for Li sensor atoms. Indeed a 3.5% discrepancy is not large for such complex, multi-electron systems and underscores the difficulty of quantifying the uncertainties in *ab initio* computations. The agreement observed between the observed R , the *ab initio* KT predictions²¹ for H_2 may indicate that the potential energy surface computed for this much simpler system is more reliable. We believe this work provides an exciting opportunity to help refine the theoretical models and associated experimental measurements for atom-based vacuum metrology.

ACKNOWLEDGMENTS

We acknowledge financial support from the Natural Sciences and Engineering Research Council of Canada (NSERC/CRSNG) and the Canadian Foundation for Innovation (CFI). This work was done at the Center for Research on Ultra-Cold Systems (CRUCS) and was supported, in part, through computational resources and services provided by Advanced Research Computing at the University of British Columbia.

V. AUTHOR DECLARATIONS

A. Conflict of Interest

K.W.M and J.L.B. have US patents 8,803,072 and 11,221,268 issued.

B. Author Contributions

Erik Frieling: Conceptualization (equal); Data curation (equal); Formal analysis (equal); Investigation (equal); Methodology (equal); Project administration (equal); Writing – original draft (equal); Writing – review & editing (equal). **Riley A. Stewart:** Conceptualization (equal); Data curation (equal); Formal analysis (equal); Investigation (equal); Methodology

(equal); Project administration (equal); Writing – original draft (equal); Writing – review & editing (equal). **James L. Booth:** Conceptualization (equal); Formal analysis (equal); Investigation (lead); Methodology (equal); Project administration (equal); Writing – original draft (equal); Writing – review & editing (equal). **Kirk W. Madison:** Conceptualization (equal); Funding acquisition (lead); Investigation (lead); Methodology (equal); Project administration (lead); Writing – original draft (equal); Writing – review & editing (equal).

C. Data Availability

The data that support the findings of this study are available from the corresponding author upon reasonable request.

Appendix A: Error Estimates

1. Effect of The Sensor Ensemble Energy Distribution

Here we discuss the systematic deviation of the R values arising from the finite trap depth and the sensor ensemble energy distribution.

To measure the total collision rate between the sensor atom and the surrounding room-temperature background gas, we monitor the loss of sensor atoms from a weakly-confining quadrupole magnetic trap. Due to the finite depth of the confining potential, a fraction of collisions will not be energetic enough to induce loss. For a sensor atom at zero energy, the loss rate Γ_{loss} deviates from the total collision rate Γ_{tot} by a trap-depth dependent function f ,

$$\begin{aligned}\Gamma_{\text{loss}}(U) &= n \langle \sigma_{\text{loss}}(U) v \rangle \\ &= n \langle \sigma_{\text{tot}} v \rangle [1 - f(U)]\end{aligned}\quad (\text{A1})$$

where $f(U)$ vanishes as the trap depth U approaches zero. The variation of f on the trap depth depends on the details of the underlying interaction potential and distribution of collisional energies. Both semi-classical and *ab-initio* calculations^{11,21} as well as experimental measurements^{11,12} have been performed to determine $f(U)$ for background species typically found in vacuum systems.

In practice, the sensor ensemble contains atoms at non-zero energy, and the effective trap depth experienced by an atom with energy E is given by $U - E$, corresponding to the energy transfer required to exceed the trap depth U . Consequently, the loss rate observed over the entire trapped ensemble is given by $\Gamma_{\text{loss}}(U)$ averaged over the distribution of trapped energies $\rho(E)$,¹³

$$\begin{aligned}\overline{\Gamma_{\text{loss}}(U)} &= n \overline{\langle \sigma_{\text{loss}}(U) v \rangle} \\ &= n \frac{\int_0^U \rho(E) \langle \sigma_{\text{loss}}(U - E) v \rangle dE}{\int_0^U \rho(E) dE}\end{aligned}\quad (\text{A2})$$

Experimental methods for determining $\rho(E)$ have been described previously and entail measuring the number of sensor atoms in the trap below some energy E , providing the cumulative distribution function $F(E) = \int_0^E \rho(E) dE$.^{11,25} Empirically, we find the distributions are reasonably well described by an offset Maxwell-Boltzmann energy distribution,

$$\rho_{\text{MB}}(\epsilon) = \Theta(\epsilon) \cdot 2 \sqrt{\frac{\epsilon}{\pi}} \left(\frac{1}{k_B T} \right)^{3/2} \exp\left(-\frac{\epsilon}{k_B T}\right) \quad (\text{A3})$$

where $\epsilon = E - E_{\text{min}}$. This describes a distribution shifted by an amount E_{min} below which no atoms are observed. The experimentally measured energy distributions for both ensembles are shown in Fig. 4. In ${}^6\text{Li}$, the unresolved hyperfine structure of the excited state involved in the D2 (${}^2S_{1/2} \rightarrow {}^2P_{3/2}$) transition inhibits sub-Doppler

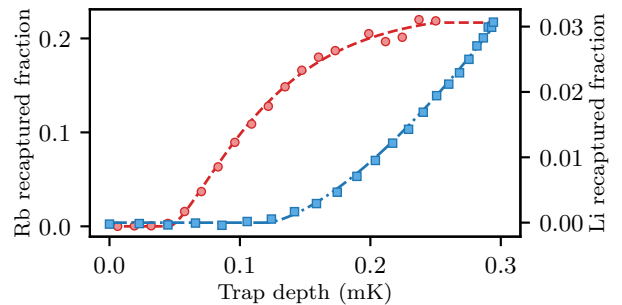


FIG. 4. Experimentally measured cumulative ensemble energy distributions for Rb (red circles) and Li (blue squares) in the magnetic trap. The Rb ensemble is held in an axial gradient of $B' = 35$ G/cm, and the trap depth is determined by the minimum frequency in a time dependent radio-frequency field sweep as described previously.^{11,25} For the Li ensemble, the axial gradient is $B' = 100$ G/cm and the trap depth is limited by field dependence of the $|1/2, -1/2\rangle$ state. The dashed lines denote the fits to an offset Maxwell-Boltzmann energy distribution $\rho_{\text{MB}}(E)$ described in Eq. A3, and the corresponding parameters are listed in Table III. For the Li ensemble, we assume an estimated temperature of $T = 1.5(5)$ mK, as described previously.

cooling mechanisms based upon differential AC stark shifts and optical pumping between Zeeman sub-levels. As such, we find energy distribution of the lithium ensemble resembles ρ_{MB} with ($3k_B T/2 \gg U$) an average energy much larger the experimental trap depths used in this work. In this limit, we are unable to determine a reasonable estimate for the ensemble temperature T using fits to eq. A3. Without sub-Doppler cooling mechanisms, and for sufficiently weak magnetic trapping gradients, one expects the energy of the trapped ensemble to be dominated by the initial kinetic energy upon loading into the magnetic trap; correspondingly, the ensemble temperature in the magnetic trap approaches the temperature of the ensemble in the MOT. We estimate the lithium ensemble temperature to be 1.5(5) mK based upon previous studies in similar experimental systems.^{32,33}

For the purposes of determining the ratio of velocity-averaged total rate coefficients R , we measure the sensor atom loss rates at exceedingly shallow trap depths, where

TABLE III. Experimental parameters describing the sensor atom energy distribution $\rho_{\text{MB}}(E)$ as determined by fits to eq. A3. The number in brackets denotes the statistical uncertainty. For the Li ensemble temperature, we assume an estimated temperature based upon previously measured ${}^6\text{Li}$ MOT temperatures conducted on similar experimental systems.^{32,33}

| Species | U (μK) | T (μK) | E_{min} (μK) |
|---------|-----------------------|-----------------------|------------------------------------|
| Rb | 125 | 54.0(1) | 46.1(1) |
| Li | 294 | 1500(500) | 116.7(8) |

the loss rate $\overline{\Gamma_{\text{loss}}(U)}$ approaches the total collision rate Γ_{tot} . To characterize the deviation of the loss rate from the total collision rate due to the non-zero trap depth U and finite-energy distribution $\rho(E)$ of the trapped ensemble, we use the trap-depth dependence model based upon *ab-initio* calculations performed by Klos and Tiesinga (KT).²¹ We note that a trap-depth dependence model based on Quantum Diffractive Universality provides similar estimates for the expected deviation in the Rb loss rate.^{11,13}

We calculate the deviation of the measured loss rate from the total collision rate by integrating $\langle\sigma_{\text{loss}}(U)v\rangle$ over the experimentally-measured energy distributions, as in eq. A2, for both trapped species. From this, we compute the deviation in R and present the results in table IV. Across all background species investigated here, the expected relative deviation $\delta R/R$ due to both a finite trap depth U and energy distribution $\rho(E)$ is less than 0.51%. The largest deviations are associated with background species where the loss rate decreases fastest with increasing trap depth. Generally, these correspond to species with a large polarizability and/or small collisional energies at room temperature.²⁶

2. Collision-induced heating

Each collision event with the background thermal gas that does not generate loss from the trapped ensemble results in momentum exchange between the collision partners. This leads to heating of the sensor atom ensemble, modifying the energy distribution $\rho(E)$.^{11,25,26,34,35} As the average loss rate over the entire ensemble depends on this distribution (eq. A2), heating modifies the observed loss rate.^{25,26,34,35} We note that, given the experimentally realized trap depth and energy distributions listed in table III, the fraction of collisions that do not result in loss is less than 0.6% across all species, significantly suppressing heating effects. Previous studies accounted for

TABLE IV. Expected systematic deviations of the R value due to finite trap depth and trapped ensemble energy distribution effects for various background species. We first find the deviation of the measured one-body loss rate from the total collision rate given the trap depth and sensor atom energy distributions for both Li and Rb. These are used to construct the predicted deviation in the value of R , relative to the value at zero trap depth, denoted R_0 .

| Bk. species | $\frac{\delta\langle\sigma_{\text{loss}}v\rangle}{\langle\sigma_{\text{tot}}v\rangle}$ (Rb/Li) [%] | $\delta R/R_0$ [%] |
|----------------|---|--------------------|
| H ₂ | -0.151/-0.017 | 0.129 |
| He | -0.058/-0.005 | 0.051 |
| Ne | -0.216/-0.023 | 0.185 |
| N ₂ | -0.316/-0.033 | 0.270 |
| Ar | -0.323/-0.035 | 0.280 |
| Kr | -0.449/-0.049 | 0.383 |
| Xe | -0.588/-0.064 | 0.500 |

heating by experimentally measuring the time-evolution of the trapped distribution.^{25,26,34,35}

For this work, we estimate the residual effects of heating by utilizing the trap-depth dependence $\langle\sigma_{\text{loss}}(U)v\rangle$ to determine the post-collisional energy probability density function P_t . As $\langle\sigma_{\text{loss}}(U)v\rangle$ represents the probability that a collision transfers an energy $E > U$ to a trapped atom, it is the complement to the cumulative density function for the post-collisional energy. Hence, the derivative of $\langle\sigma_{\text{loss}}(U)v\rangle$ yields P_t ,

$$P_t(U) \equiv \frac{d}{dU}\langle\sigma_{\text{loss}}(U)v\rangle. \quad (\text{A4})$$

For sufficiently low trap depths, the energy distribution of the trapped ensemble can be approximated by the contributions from two sub-ensembles,

$$\rho(E, t) \simeq \rho_0(E, t) + \rho_1(E, t) \quad (\text{A5})$$

where ρ_0 and ρ_1 correspond to trapped populations that have experienced 0 or 1 collision events respectively. In principle, higher order terms exist but are negligible at the trap depths considered here. Our formulation to account for heating follows a rigorous treatment discussed previously^{34,35} and recently applied to correct the measurements of Barker *et al.*²³. Both populations are depleted at a rate of $\exp(-\Gamma t)$, with the small fraction of heating collision events transferring particles from ρ_0 to ρ_1 at a rate of Γt . The energy distribution of the heated sub-ensemble ρ_1 is the sub-ensemble ρ_0 modified by the post-collisional energy distribution P_t . Specifically, ρ_1 is the convolution of ρ_0 and P_t ,

$$\rho_1(E) = \int_0^E P_t(E - E')\rho_0(E')dE'. \quad (\text{A6})$$

Hence, the approximate time-evolution of the trapped distribution is governed by,

$$\rho(E, t) \simeq e^{-\Gamma t} \left[\rho_0(E) + \Gamma t \int_0^E P_t(E - E')\rho_0(E')dE' \right]. \quad (\text{A7})$$

Using the KT trap-depth dependence model, we compute time-evolution of the ensemble energy distribution, from which the cumulative population below a given trap depth U (f_{recap}) can be determined as a function of time.

In accordance with our exceedingly low trap depths (and hence small number of heating collisions), we find the loss rates $\overline{\Gamma_{\text{loss}}}$ derived from a two-point measurement scheme, including ensemble heating, are modified by less than 0.004% across all background species for the Rb ensemble, and less than 0.0004% for the Li ensemble given our experimental conditions. Table V presents the combined relative deviation $\delta R/R$ due to ensemble heating. Across all background species, the expected deviations due to ensemble heating are less than 0.004%.

TABLE V. Estimated systematic deviation due to ensemble heating for various background species, given the experimental conditions given in table III.

| Bk. species | $\frac{\delta\overline{\Gamma_{\text{loss}}}}{\overline{\Gamma_{\text{loss}}}}$ (Rb/Li) [10 ⁻⁴ %] | $\delta R/R$ [10 ⁻⁴ %] |
|----------------|---|-----------------------------------|
| H ₂ | -2.43/-0.04 | -2.39 |
| He | -0.357/-0.004 | -0.353 |
| Ne | -5.01/-0.06 | -4.95 |
| N ₂ | -10.43/-0.14 | -10.29 |
| Ar | -11.28/-0.16 | -11.12 |
| Kr | -21.12/-0.29 | -20.83 |
| Xe | -36.17/-0.50 | -35.67 |

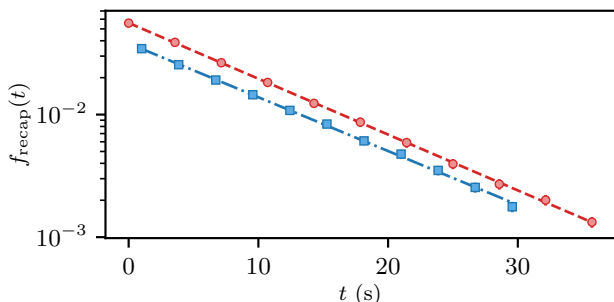


FIG. 5. Typical atom loss curves for magnetically-trapped Rb (red circles) and Li (blue squares) ensembles subject to collision-induced loss due to a background thermal gas of Ne. The dashed and dash-dot curves denote fits to a one-body loss rate model providing $\Gamma_{\text{loss}}^{\text{Rb}} = 0.106(1)$ Hz and $\Gamma_{\text{loss}}^{\text{Li}} = 0.100(1)$ Hz for Rb or Li respectively. We observe no statistically-significant evidence of two-body or higher order loss.

3. Density-dependent losses

Trapped atoms are subject to a number of loss channels alongside to those generated by collisions with the thermal background gas. These include Majorana spin-flips, a process by which atoms undergo a non-adiabatic transition to an untrappable (high-field seeking) spin state. In addition, there are higher n -body ($n \geq 2$) elastic and inelastic losses that depend on the intra-trap density. The differential atom loss per unit time is given by,

$$\frac{dn}{dt} = -\Gamma n - L_2 n^2 + \mathcal{O}(n^3) \quad (\text{A8})$$

where Γ and L_2 represents the one and two-body rate coefficients respectively, including inelastic and elastic losses. For typical intra-trap densities, terms of order n^3 and above can be neglected. Example loss rate curves are shown in Fig. 5; experimentally, we observe no statistically-significant evidence of two-body or higher order losses. We also observe no significant deviations between measurements of R using loss rate curves sampled with $N = 10$ points equally spaced between $t = 0$ and $t = 1.5/\Gamma$, and those taken using a two-point measurement scheme. Both observations serve to support the

validity of the two-point measurement scheme for determining the one-body loss rate.

We estimate an upper-bound for the systematic deviation in the inferred one-body loss rate measured from a two-point measurement scheme due to additional density-dependent losses by calculating the shift in the atom recapture due to this loss channel, constrained by our experimentally-measured loss rate curves. As our detection method measures total atom number $N = \int n d\mathbf{r}$, we integrate eq. A8 over the spatial trapping volume to find,

$$\frac{dN}{dt} = -\Gamma N - \tilde{\beta} N^2 \quad (\text{A9})$$

dropping higher-order terms, and where $\tilde{\beta}$ is given by,

$$\tilde{\beta}(t) = \beta \frac{\int_{\Omega} n^2(\mathbf{r}, t) d\mathbf{r}}{(\int_{\Omega} n(\mathbf{r}, t) d\mathbf{r})^2} \quad (\text{A10})$$

where Ω denotes the energetically-accessible spatial volume for particles retained in the magnetic trap. We assume that $\tilde{\beta}(t) \simeq \tilde{\beta}(0)$ is approximately constant over the trapping duration t , under which the solution to eq A9 is given by,

$$N(t) = \frac{N_0 e^{-\Gamma t}}{1 + \tilde{\beta} N_0 / \Gamma (1 - e^{-\Gamma t})} \quad (\text{A11})$$

where N_0 is the initial atom number at $t = 0$. For the data presented in Fig. 5, we find $\tilde{\beta}_{\text{Rb}} = -0.002(63)$ and $\tilde{\beta}_{\text{Li}} = -0.07(17)$ for Rb and Li respectively, both statistically consistent with zero. We note that as ⁶Li is fermionic and the magnetically trapped atoms are in identical spin states, two-body collisions (and thus density-dependent losses) are forbidden for s-wave collisions and frozen out for p-wave collisions at the sensor-atom energies for these measurements.²⁶ We thus set $\tilde{\beta}_{\text{Li}} = 0$, and assume an upper bound on $\tilde{\beta}_{\text{Rb}} \leq 0.061$ for the Rb ensemble.

In order to calculate an upper bound on the resulting shift in R , we perform a Monte-Carlo simulation of sampling 10 loss rates across a random selection of one-body loss rates between 0.07-0.4 Hz, corresponding to experimentally-relevant values (see Fig. 2). At each pressure, the loss rate from both the Rb and Li ensembles is calculated from the atom number at two trapped times $t = 0$ and $t = 1.5/\Gamma$, as determined by eq. A11, with the $\tilde{\beta}$ values for the two species specified above. The value of R is then determined by fits to a linear model using ODR. After many such samples, we observe a relative deviation in the mean value of R that is less than -0.05%.

4. Background temperature

The thermally-averaged total collision rate coefficient $\langle \sigma_{\text{tot}} v \rangle$ depends on temperature of the background thermal gas in the vicinity of the magnetically-trapped sen-

sor atoms. Writing this quantity in terms of an integral over the speed distribution of impinging background particles,¹¹

$$\langle \sigma_{\text{tot}} v \rangle = 4\pi \int_0^\infty v^3 \rho_{\text{bk}}(v, T, m_b) \sigma_{\text{tot}}(v) dv \quad (\text{A12})$$

where the speed of the thermal background is assumed to be Maxwell-Boltzmann distributed,

$$\rho_{\text{bk}}(v, T, m_b) = \sqrt{\frac{2}{\pi}} \left(\frac{m_b}{k_B T} \right)^{3/2} \exp\left(-\frac{mv^2}{2k_B T}\right) \quad (\text{A13})$$

and m_b is the mass of the background particle. To estimate the magnitude of the expected deviation, we approximate the leading-order dependence of $\langle \sigma_{\text{tot}} v \rangle$ using the Jeffreys-Born approximation for the elastic scattering phase shifts, for which one can derive for a van-der Waals potential of the form $V(r) = -C_6/r^6$,¹¹

$$\begin{aligned} \langle \sigma_{\text{tot}} v \rangle &= 8.494636 \left(\frac{C_6}{\hbar v_p} \right)^{\frac{2}{5}} v_p + 7.19729 \left(\frac{\hbar}{\mu} \right) \left(\frac{C_6}{\hbar v_p} \right)^{\frac{1}{5}} \\ &= \langle \sigma_{\text{tot}} v \rangle_0 + \langle \sigma_{\text{tot}} v \rangle_1 \end{aligned} \quad (\text{A14})$$

where $v_p = \sqrt{2k_B T/m_b}$ is the most probable speed given the background thermal distribution in eq. A13. We thus find,

$$\begin{aligned} \delta \langle \sigma_{\text{tot}} v \rangle &= \frac{3}{10} \frac{\delta T}{T} \langle \sigma_{\text{tot}} v \rangle_0 - \frac{1}{10} \langle \sigma_{\text{tot}} v \rangle_1 \frac{\delta T}{T} \\ &= \frac{3}{10} \frac{\delta T}{T} \langle \sigma_{\text{tot}} v \rangle - \frac{2}{5} \frac{\delta T}{T} \langle \sigma_{\text{tot}} v \rangle_1 \end{aligned} \quad (\text{A15})$$

The relative shift in $\langle \sigma_{\text{tot}} v \rangle$ is then given by,

$$\frac{\delta \langle \sigma_{\text{tot}} v \rangle}{\langle \sigma_{\text{tot}} v \rangle} = \frac{3}{10} \frac{\delta T}{T} - \frac{2}{5} \frac{\delta T}{T} \frac{\langle \sigma_{\text{tot}} v \rangle_1}{\langle \sigma_{\text{tot}} v \rangle}. \quad (\text{A16})$$

From the above, one can construct the resulting shift in R ,

$$\begin{aligned} \frac{\delta R}{R} &= \frac{\delta \langle \sigma_{\text{tot}} v \rangle_{\text{Li}}}{\langle \sigma_{\text{tot}} v \rangle_{\text{Li}}} - \frac{\delta \langle \sigma_{\text{tot}} v \rangle_{\text{Rb}}}{\langle \sigma_{\text{tot}} v \rangle_{\text{Rb}}} \\ &= \frac{2}{5} \frac{\delta T}{T} \left[\frac{\langle \sigma_{\text{tot}} v \rangle_{\text{Rb},1}}{\langle \sigma_{\text{tot}} v \rangle_{\text{Rb}}} - \frac{\langle \sigma_{\text{tot}} v \rangle_{\text{Li},1}}{\langle \sigma_{\text{tot}} v \rangle_{\text{Li}}} \right] \end{aligned} \quad (\text{A17})$$

Given calculated C_6 values found in literature^{21,30}, and an estimated maximum variation in the background temperature of $\delta T = 2$ K, we find estimated relative shift $\delta R/R$ due to fluctuations in the background temperature. The results are presented in table A 4. Across all species, the relative deviation $\delta R/R$ is less than 0.012%. We note that the order of magnitude of the above predicted deviation is consistent those calculated using the KT model across all species.²¹

5. Contributions of other background gases

During the measurement, we monitor the partial pressure of background gases in our system using an RGA.

TABLE VI. Estimated systematic deviation due to variations in the temperature of the background thermal gas in the vicinity of the trapped sensor atoms. The values of C_6 are given in atomic units, where E_h is the Hartree energy and a_0 is the bohr radius. Values for H₂ and N₂ taken from Klos *et al.*, with values for all other species taken from Jiang *et al.*^{21,30}

| Bk. species | $C_6 (E_h a_0^6)$ (Rb/Li) | $\delta R/R_0$ [%] |
|----------------|------------------------------|--------------------|
| H ₂ | 148.8 / 82.8 | 0.004 |
| He | 44.7 / 22.5 | 0.006 |
| Ne | 88.2 / 43.8 | 0.008 |
| N ₂ | 349 / 184 | 0.008 |
| Ar | 337 / 174 | 0.008 |
| Kr | 499 / 260 | 0.01 |
| Xe | 782 / 411 | 0.012 |

If the partial pressure of gases other than the test gas is random from shot-to-shot, this would only contribute to the statistical noise. However, if there is some correlated increase, for example due to contamination of the test gas before it is leaked in or due to the changing gas load affecting the behaviour of the ion pumps, NEG's or the turbo pump, this would show up as a shift in the measured value of R . Here, we estimate the contribution of these background gas density changes $\Delta n_i = n_i - n_i^0$ during the measurement, assuming the worst case scenario of a perfect correlation with the change in the test gas density $\Delta n_X = n_X - n_X^0$.

We start by writing R in terms of Δn_i and the values of $\langle \sigma_{\text{tot}} v \rangle$ for Li and Rb:

$$\begin{aligned} R &= \frac{\Gamma_{\text{Li}} - \Gamma_{(\text{Li},0)}}{\Gamma_{\text{Rb}} - \Gamma_{(\text{Rb},0)}} \\ &= \frac{\sum (n_i - n_i^0) \langle \sigma_{\text{tot}} v \rangle_{\text{Li}+i}}{\sum (n_i - n_i^0) \langle \sigma_{\text{tot}} v \rangle_{\text{Rb}+i}} \end{aligned} \quad (\text{A18})$$

Pulling out a factor of R_X , and expanding assuming $\Delta n_i/\Delta n_X \ll 1$ yields

$$\begin{aligned}
R &= R_X \frac{1 + \sum_{i \neq X} \frac{\Delta n_i \langle \sigma_{\text{tot}} v \rangle_{\text{Li}+i}}{\Delta n_X \langle \sigma_{\text{tot}} v \rangle_{\text{Li}+X}}}{1 + \sum_{i \neq X} \frac{\Delta n_i \langle \sigma_{\text{tot}} v \rangle_{\text{Rb}+i}}{\Delta n_X \langle \sigma_{\text{tot}} v \rangle_{\text{Rb}+X}}} \\
&= R_X \left(1 + \sum_{i \neq X} \frac{\Delta n_i \langle \sigma_{\text{tot}} v \rangle_{\text{Li}+i}}{\Delta n_X \langle \sigma_{\text{tot}} v \rangle_{\text{Li}+X}} \right) \left(1 - \right. \\
&\quad \left. \sum_{i \neq X} \frac{\Delta n_i \langle \sigma_{\text{tot}} v \rangle_{\text{Rb}+i}}{\Delta n_X \langle \sigma_{\text{tot}} v \rangle_{\text{Rb}+X}} + \mathcal{O} \left[\left(\frac{\Delta n_i}{\Delta n_X} \right)^2 \right] \right) \\
&= R_X \left(1 + \sum_{i \neq X} \left\{ \frac{\Delta n_i \langle \sigma_{\text{tot}} v \rangle_{\text{Li}+i}}{\Delta n_X \langle \sigma_{\text{tot}} v \rangle_{\text{Li}+X}} \right. \right. \\
&\quad \left. \left. - \frac{\Delta n_i \langle \sigma_{\text{tot}} v \rangle_{\text{Rb}+i}}{\Delta n_X \langle \sigma_{\text{tot}} v \rangle_{\text{Rb}+X}} + \mathcal{O} \left[\left(\frac{\Delta n_i}{\Delta n_X} \right)^2 \right] \right\} \right). \tag{A19}
\end{aligned}$$

We rewrite this in terms of the change in the partial pressure of the i^{th} background species $\Delta P_i = \Delta n_i k_B T$ and $R_i = \langle \sigma_{\text{tot}} v \rangle_{\text{Li}+i} / \langle \sigma_{\text{tot}} v \rangle_{\text{Rb}+i}$:

$$R = R_X + \delta_R^P \tag{A20}$$

$$\delta_R^P = R_X \left(\sum_{i \neq X} \left\{ \frac{\Delta P_i}{\Delta P_X} \frac{\langle \sigma_{\text{tot}} v \rangle_{\text{Li}+i}}{\langle \sigma_{\text{tot}} v \rangle_{\text{Li}+X}} \left[1 - \frac{R_X}{R_i} \right] \right\} \right) \tag{A21}$$

This analysis is limited to gases for which we know R_i . Fortunately, the only mass numbers that show up in significant quantities on the RGA are 2 (H_2), 40 (Ar) and 28 (N_2).

The RGA is not well calibrated to give quantitative measurements of the pressure, and there is differential pumping between the RGA and the magnetic trap. Thus we start by estimating a correction factor $k_{\text{RGA}} = P_{\text{atoms}} / P_{\text{RGA}}$ relating the pressure measured by the RGA P_{RGA} to the pressure at the magnetic trap P_{atoms} . For each test gas, we use the known values of $\langle \sigma_{\text{tot}} v \rangle_{\text{Li}+X}$ and the measured loss rates to calculate ΔP_X . This assumes that the test gas is the dominant contribution to the loss rate and is justified for these measurements.

We compare this to P_{RGA} to calculate the correction factor k_{RGA} for all 7 gases we investigated. Finally, we calculated ΔP_i for the background gases, and estimate the contribution δ_R^P , as shown in table VII.

Since Helium has by far the lowest R value, it provides a relatively large contribution to δ_R^P . We include a column showing the values of δ_R^P with the contribution of Helium removed. From table VII, it is clear that the contribution of these pressure fluctuations is well below the statistical error σ^{stat} .

TABLE VII. Estimated deviation δ_R^P/R of the measured R values due to the change in the partial pressure of gases other than the test gas with pressure change δP_X . The value of δ_R^P/R with the contribution from He removed is also shown, since this is the largest negative contribution due to the low value $R_{\text{Li}+\text{He}}$. The deviations are well below the statistical error σ^{stat} .

| Test gas [Torr] | ΔP_X | δ_R^P/R [%] | δ_R^P/R (w/o He) [%] |
|-----------------|----------------------|--------------------|-----------------------------|
| H_2 | 3.4×10^{-9} | -0.067 | 8.8×10^{-4} |
| He | 7.2×10^{-9} | 0.002 | |
| Ne | 1.0×10^{-8} | -0.023 | 0.335 |
| N_2 | 4.0×10^{-9} | -0.018 | 0.021 |
| Ar | 8.1×10^{-9} | -0.009 | 0.120 |
| Kr | 9.4×10^{-9} | -0.012 | 0.062 |
| Xe | 9.5×10^{-9} | -0.008 | 0.135 |

Appendix B: A discussion of the origins of the observed discrepancies in R

In this work we have observed that the $R_{6,87} = \langle \sigma_{\text{tot}} v \rangle_{6\text{Li}+X} / \langle \sigma_{\text{tot}} v \rangle_{87\text{Rb}+X}$ value is remarkably constant for heavier collision partners. Indeed, the corresponding $R_{7,87}^{\text{KT}}$ computed by Klos and Tiesinga (KT) also demonstrate this same behaviour. However, the average R values for these two differ systematically by 3.5(5)% for the heavy collision partners: $\langle R_{6,87} \rangle = 0.7965(9)$ and $\langle R_{7,87}^{\text{KT}} \rangle = 0.770(5)$. The $R_{6,87}$ reported here have been corrected for finite trap depth effects (an effect that is less than 0.5% in all cases), and the $R_{7,87}^{\text{KT}}$ have been matched to our experimental ambient temperature following the KT prescription.²¹ The remaining systematic measurement errors (type B), as shown in Appendix A, have been estimated to be less than 0.15% in this work and the estimated statistical errors on our individual $R_{6,87}$ are less than 0.8%. Thus, we face the conclusion that the *systematic* 3.5% discrepancy is significant and must be due to some other, unaccounted for, source.

One intriguing possibility is that the discrepancies arise from the potential energy surfaces (PES) (i.e. potential energy functions) used in the quantum scattering computations (QSC) which are the basis of the $R_{7,87}^{\text{KT}}$ estimates. Accurate determination of the interaction potential (especially at short range) is difficult, especially when the number of electrons in the collision complex is large, as it involves solving a computationally complex many-body quantum problem. In many cases, exact diagonalization is not possible and approximations are employed which may not accurately reflect the true potential.

To illustrate this point, it is helpful to examine the case of H_2 collisions with the sensor atoms. Recent work investigated the variation of the *ab initio* $\text{Li}+\text{H}_2$ potentials that resulted from various levels of approximation, allowing the authors to converge on a PES that had a small underlying uncertainty¹⁷. For this case, the corresponding quantum scattering computation value, $R_{7,87}^{\text{KT}} = 0.82(3)$,

agrees with our value here $R_{6,87} = 0.824(5)$ and with our previous measurement, $R_{6,87}^{\text{SEXP}} = 0.83(5)$.

However, the next simplest collision partner to model, He, yielded $R_{6,87} = 0.729(6)$ compared to $R_{7,87}^{\text{KT}} = 0.69(2)$, a 2σ discrepancy. The $R_{6,87}$ experimental result does, however, agree with the value deduced from the measurements by Barker *et al*, $R_{7,87}^{\text{BEXP}} = 0.73(2)$.

To provide some guidance on this interpretation (that the potential energy surfaces used may have errors), we investigate here how the changes of potential may manifest in loss rate measurements, and we test which sensor species is most sensitive to these changes. As stated in the main text, the collision-induced trap loss rate is characterized by,

$$\Gamma = n \langle \sigma_{\text{tot}} v \rangle \quad (\text{B1})$$

for shallow traps. Here n is the density of background particles impinging on the trapped atoms, v is the relative speed of the collisions – the speed of the impinging particles on our cold ensembles –, and $\sigma_{\text{tot}}(v)$ is the speed-dependent total elastic collision cross-section. The brackets, $\langle \rangle$, indicate that one measures the average loss rate of many collision partners striking the trapped sensor ensemble from different directions and with a Maxwell-Boltzmann speed distribution (MB) set by the ambient temperature of the test apparatus and the mass of the impinging particles. Quantum scattering computations (QSC) can be used to determine the collision cross-section, $\sigma(v)$, provided sufficiently physically - realistic potential energy surfaces, or in simpler cases, potential energy functions are known *a priori*.

In their simplest form the potential energy functions describing the collision dynamics consist of a short range, repulsive region for inter-species separations, $r < r_c$, and a long-range van der Waals attraction, $-C_6/r^6 - C_8/r^8 - C_{10}/r^{10}$ for $r > r_c$. *Ab initio* calculations of the van der Waals coefficients, C_n , have been performed for a wide range of collision partners. (For example see^{30,36}.) The core portion of the potential is a greater challenge to model.

Fortunately, by their nature, the shallow trap loss rate measurements are most sensitive to the long-range van der Waals-mediated, glancing collisions. Following³⁷, the elastic collision cross-section between two species, $\sigma(v)$, is a smoothly decreasing cross-section with increasing relative velocity, v . For a simple potential, $V(R) = -C_6/r^6$, the prediction is³⁷,

$$\sigma_{C_6}(v) \approx 8.0828 \left(\frac{C_6}{\hbar v} \right)^{\frac{2}{5}} \quad (\text{B2})$$

which leads to a cross-section decreasing as $v^{2/5}$. This picture is modified by the presence of so-called glory scattering, partial waves characterized by low angular momentum values, L , which produce scattering in the forward direction and result in interference oscillations about the smooth, decreasing cross-section, $\sigma_{C_6}(v)$. The

pattern of these glory oscillations depends on the details of the core portion of the potential describing the collision interaction. In general, the glory oscillations have the following characteristics³⁷,

1. The number of oscillations per unit velocity decreases with a decreasing reduced mass of collision partners.
2. The amplitude of the oscillations increases with a decreasing reduced mass of collision partners.

These features are illustrated in Fig. 6, which shows scaled plots of quantum scattering computations (QSC) of $\sigma(v)$ for Li-Xe and Rb-Xe collisions, based on the interaction potentials published by Kłos *et al*²¹. We observe the larger oscillation amplitude for the Li-Xe cross-sections compared to those for Rb-Xe, and the lower oscillation rate with speed for Li-Xe.

One of the advantages of measuring $\langle \sigma_{\text{tot}} v \rangle$ is that the effects of these glory oscillations are at least partially mitigated by the averaging process. Namely,

$$\langle \sigma_{\text{tot}} v \rangle = \int 4\pi v^2 dv (v \cdot MB(v) \cdot \sigma(v)). \quad (\text{B3})$$

Here $MB(v)$ is the Maxwell-Boltzmann speed distribution of the impinging collision partners. If there are numerous low-amplitude oscillations over the range of the integration, the glory oscillations, and, subsequently, the information they carry about the core potential, are suppressed. This leads to the universality of the $\langle \sigma_{\text{tot}} v \rangle$ values discussed previously.¹¹⁻¹³

To underscore the difference in the behaviour between Li-Xe and Rb-Xe collisions, the products, $(v \cdot MB(v) \cdot \sigma(v))$, as a function of v for these species are shown in Fig. 7. One observes that the Rb-Xe plot approximates the ideal case with many small amplitude oscillation over the velocity range selected by the MB function. The Li-Xe plot, however, shows only a few large-amplitude oscillations over the same velocity range. Thus, one expects that the details of the core portion of the potential will not contribute significantly to $\langle \sigma_{\text{tot}} v \rangle_{\text{Rb-Xe}}$. By contrast, the details of the core will likely persist for the Li-Xe collisions. Thus, one might expect that changing the details of the core used in the QSC used to compute $\sigma(v)$ will lead to changes in the value of $\langle \sigma_{\text{tot}} v \rangle$.

Thus, it is plausible that a large portion of the discrepancies between the measured values of $R_{6,87}$ presented here and the values derived from the theoretical QSC $\langle \sigma_{\text{tot}} v \rangle$ of Kłos and Tiesinga²¹ used in $R_{7,87}^{\text{KT}}$ arise from details of the core of the interaction potentials between Li and its collision partners used in the theoretical estimates. While it is beyond the scope of this paper to investigate the detailed properties of the potentials, three tests were carried out. We note that although the computations presented below were calculated using an ambient

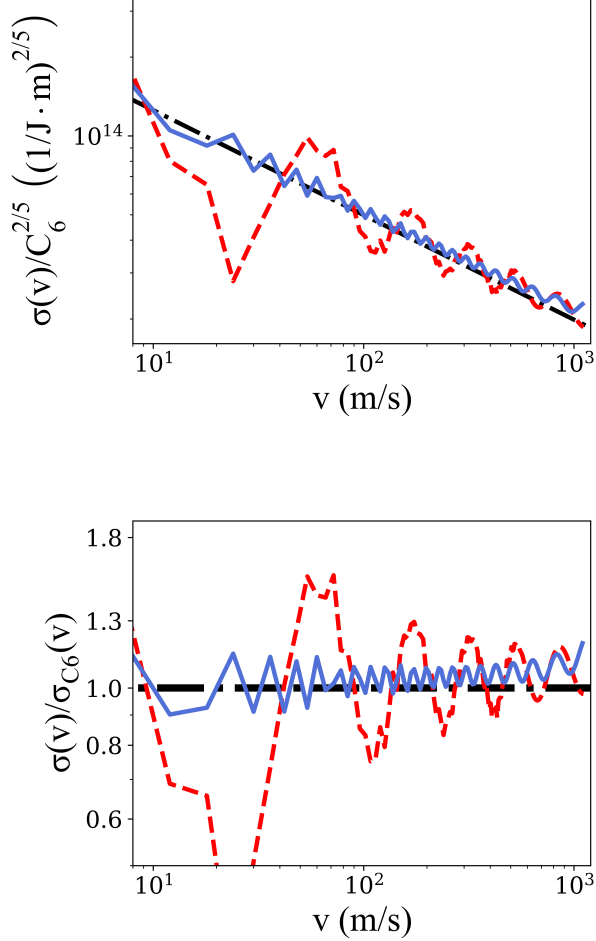


FIG. 6. Top panel: Plot of the normalized elastic cross-sections normalized, $\sigma(v)/C_6^{2/5}$ versus v for Rb-Xe (blue solid trace), Li-Xe (red dashed trace) and the prediction from Eq. B2 for a purely $-C_6/r^6$ potential (black dash-dot trace). The computations, based on the interaction potentials published by Klos *et al*²¹, demonstrate the more pronounced and lower frequency glory oscillations for a light collision partner, Li, and compared to a heavy one, Rb, interacting with the same background gas species, Xe. Bottom panel: Plot of $\sigma(v)/\sigma_{C_6}(v)$ versus v . This normalization removes the purely C_6 long range portion of the computed cross-sections. The blue solid trace corresponds to Rb-Xe and the red dashed trace to Li-Xe. The presence of the long range C_8 and C_{10} terms in the KT potentials used in the QSC lead to the upward trends at the high relative speed end of the plots.

temperature of 21 C (294K) rather than the experimental temperature of 25 C (298K), the qualitative findings presented here are unaffected by this choice.

First, we validate the hypothesis that some of the information about the core repulsion persists for the Li-Xe $\langle\sigma_{\text{tot}} v\rangle$ (and, by extension, for other Li-X collision

| Species | $\langle\sigma_{\text{tot}} v\rangle_{\text{KT}}$ | $\langle\sigma_{\text{tot}} v\rangle_{\text{SC}}$ | $\langle\sigma_{\text{tot}} v\rangle_{\text{SC}} / \langle\sigma_{\text{tot}} v\rangle_{\text{KT}}$ |
|-------------------|---|---|---|
| Li-N ₂ | 2.63 | 2.69 | 1.022 |
| Li-Ar | 2.33 | 2.36 | 1.013 |
| Li-Kr | 2.14 | 2.20 | 1.028 |
| Li-Xe | 2.24 | 2.29 | 1.022 |
| Rb-N ₂ | 3.45 | 3.47 | 1.006 |
| Rb-Ar | 3.031 | 3.023 | 0.997 |
| Rb-Kr | 2.79 | 2.78 | 0.996 |
| Rb-Xe | 2.87 | 2.88 | 1.003 |

TABLE VIII. The QSC $\langle\sigma_{\text{tot}} v\rangle_{\text{KT}}$ values based on the potentials reported by²¹ compared to SC computations, $\langle\sigma_{\text{tot}} v\rangle_{\text{SC}}$, at a temperature of 21 C. Column 4 shows the ratio of the SC to the QSC $\langle\sigma_{\text{tot}} v\rangle$. There is a systematic difference of 2% between the QSC and SC values for the Li collisions compared to the near perfect agreement for the Rb computations. (Note all $\langle\sigma_{\text{tot}} v\rangle$ values have units of $\times 10^{-15} \text{ m}^3/\text{s}$.)

partners) while this information is absent in the corresponding Rb-Xe QSC. To illustrate this point, a semi-classical (SC) approximation was used which describes a solely long-range van der Waals interaction potential, $-C_6/r^6 - C_8/r^8 - C_{10}/r^{10}$. The corresponding Jeffreys-Born elastic scattering phase shifts for each C_n term are³⁷,

$$\eta_n(L, k) = -p(n) \left(\frac{\mu C_n}{\hbar^2} \right) \frac{k^{n-2}}{L^{n-1}} \quad (\text{B4})$$

where

$$p(n) = \frac{1}{2} \Gamma \left(\frac{1}{2} \right) \cdot \frac{\Gamma \left(\frac{1}{2} (n-1) \right)}{\Gamma \left(\frac{1}{2} n \right)}. \quad (\text{B5})$$

With this prescription the semi-classical (SC) total collision cross-sections, $\langle\sigma_{\text{tot}} v\rangle_{\text{SC}}$, were computed using the C_n values published by KT²¹. These are compared to the corresponding KT QSC values, $\langle\sigma_{\text{tot}} v\rangle_{\text{KT}}$ in Table VIII. The fourth column shows the ratio of SC to QSC values. Since the SC description contains no core repulsion, the ratio is a measure of how thoroughly the velocity averaging suppresses the glory effects of the core on $\langle\sigma_{\text{tot}} v\rangle$. We see that the ratio is very close to 1 for the Rb-X while the Li-X SC values are approximately 2% larger than the KT QSC values, indicating the persistence of some details of the core repulsion in the Li-X computations (in this case reducing $\langle\sigma_{\text{tot}} v\rangle$ through destructive interference).

Second, the sensitivity of the Rb-Ar QSC of $\langle\sigma_{\text{tot}} v\rangle$ to changes in the depth of the interaction potential, D_e , was examined. For this test the Rb-Ar potential described by Medvedev *et al*³⁸ was used in the computations since it is written in a form which allows the depth of potential, D_e , to be varied easily and yields a value of $\langle\sigma_{\text{tot}} v\rangle$ nearly identical to the value determined by the KT potential: $\langle\sigma_{\text{tot}} v\rangle_{\text{Med}} = 3.04 \times 10^{-15} \text{ m}^3/\text{s}$ compared to $\langle\sigma_{\text{tot}} v\rangle_{\text{KT}} = 3.03 \times 10^{-15} \text{ m}^3/\text{s}$ at $T = 21 \text{ C}$. Changing the potential depth by $\pm 10\%$ led to no difference in $\langle\sigma_{\text{tot}} v\rangle$ on the 0.1% level. (See Table IX.) Again, this supports the hypothesis that $\langle\sigma_{\text{tot}} v\rangle$ is immune to

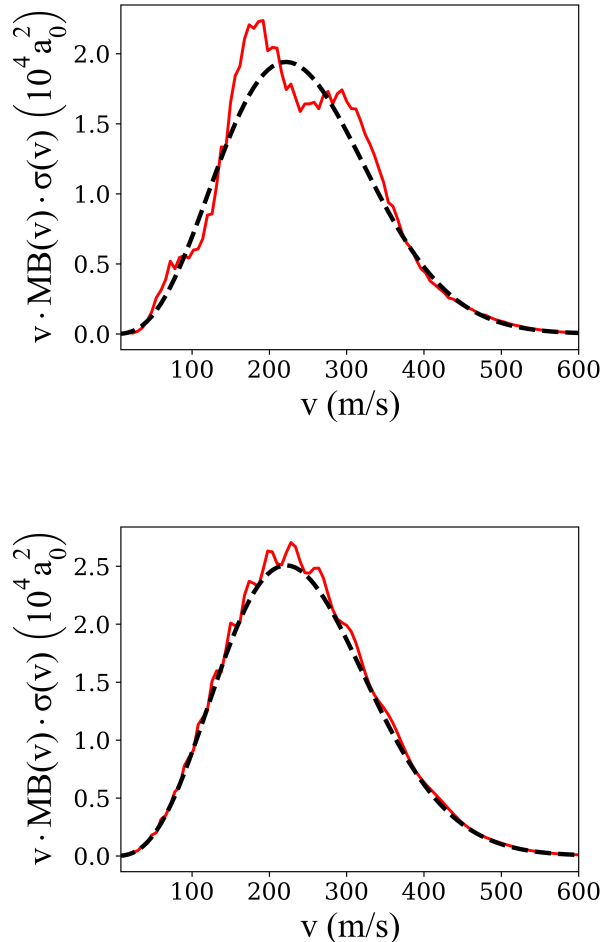


FIG. 7. The upper panel is a plot of the product $v \cdot MB \cdot \sigma(v)$ versus v for Li-Xe while the lower panel is the corresponding plot for Rb-Xe. The solid red traces are the full quantum scattering computations (QSC) based on the KT potentials²¹, while the black dashed traces are the $\sigma_{C6}(v)$ predictions (Eq. B2). The latter contain no glory oscillation effects and indicate a single term, purely the long-range interaction potential.

changing this detail of the core potential for Rb-Ar collisions. A similar comparison for Li-Ar collisions was not performed as Medvedev has not published an equivalent model for this collision pair. The KT published models are not amenable to parameter manipulation.

Third, the KT description of the interaction potential for Li-Xe²¹ stitches together the short-range or core portion of the potential with the long-range van der Waals potential at an interspecies location labeled $r = r_c$. In KT's work²¹, $r_c = 18.5 a_0$ for Li-Xe. Three different r_c values were selected and the QSC for $\langle \sigma_{\text{tot}} v \rangle$ were carried out to observe the shift in its value. The results are summarized in Table X. We observe a variation on the

| D_e (cm^{-1}) | $\langle \sigma_{\text{tot}} v \rangle$ ($\times 10^{-15} \text{m}^3/\text{s}$) |
|----------------------------|---|
| -41 | 3.041 |
| -38 (nom. value) | 3.040 |
| -35 | 3.038 |

TABLE IX. The $\langle \sigma_{\text{tot}} v \rangle$ values computed for Rb-Ar collisions varying the potential depth, D_e , using the Medvedev³⁸ potential description. We see that varying the depth by $\pm 10\%$ changes the value by less than 0.1%.

| r_c (a_0) | $\langle \sigma_{\text{tot}} v \rangle$ ($\times 10^{-15} \text{m}^3/\text{s}$) |
|-------------------|---|
| 13.9 | 2.22 |
| 18.5 (nom. value) | 2.23 |
| 37.0 | 2.24 |

TABLE X. The variation in the Li-Xe $\langle \sigma_{\text{tot}} v \rangle$ value as a function of r_c , the location where the core and long-range van der Waals portions of the KT potentials connect. It is clear that the $\langle \sigma_{\text{tot}} v \rangle$ values are not sensitive to this parameter. Neither the core potential nor the long range portion of the potential were varied in these computations.

order of 1% requires very large changes in this parameter, indicating that shifting this parameter is not effective at changing the glory contributions to $\langle \sigma_{\text{tot}} v \rangle$. We believe this test rules out the long-range portion of the potentials as being responsible for the discrepancies observed between our reported $R_{6,87}$ and $R_{7,87}^{\text{KT}}$. Thus, we hypothesize that the core potentials described by Kłos *et al*²¹ may need to be modified by adjusting the width and location of the potential minimum, and/or by adjusting the shape of the very short range repulsion curve to increase the computed $\langle \sigma_{\text{tot}} v \rangle$ values. If this hypothesis is correct, then this provides a rare and exciting opportunity to investigate the shape of the short-range portion of the interaction potential experimentally.

- ¹J. Booth, D. E. Fagnan, B. G. Klappauf, K. W. Madison, and J. Wang, Method and device for accurately measuring the incident flux of ambient particles in a high or ultra-high vacuum environment (2011).
- ²K. W. Madison, A cold atom based UHV pressure standard, personal communication (2012).
- ³T. Arpornthip, C. A. Sackett, and K. J. Hughes, *Physical Review A* **85**, 33420 (2012).
- ⁴J.-P. Yuan, Z.-H. Ji, Y.-T. Zhao, X.-F. Chang, L.-T. Xiao, and S.-T. Jia, *Applied Optics* **52**, 6195 (2013).
- ⁵R. W. G. Moore, L. A. Lee, E. A. Findlay, L. Torralbo-Campo, G. D. Bruce, and D. Cassettari, *Review of Scientific Instruments* **86**, 093108 (2015).
- ⁶V. B. Makhalov, K. A. Martiyanov, and A. V. Turlapov, *Metrologia* **53**, 1287 (2016).
- ⁷V. B. Makhalov and A. V. Turlapov, *Quantum Electronics* **47**, 431 (2017).
- ⁸J. Scherschligt, J. A. Fedchak, D. S. Barker, S. Eckel, N. Klimov, C. Makrides, and E. Tiesinga, *Metrologia* **54**, S125 (2017).
- ⁹J. Scherschligt, J. A. Fedchak, Z. Ahmed, D. S. Barker, K. Douglass, S. Eckel, E. Hanson, J. Hendricks, N. Klimov, T. Purdy, J. Ricker, R. Singh, and J. Stone, *Journal of Vacuum Science & Technology A* **36**, 040801 (2018).
- ¹⁰J.-f. Xiang, H.-n. Cheng, X.-k. Peng, X.-w. Wang, W. Ren, J.-w. Ji, K.-k. Liu, J.-b. Zhao, L. Li, Q.-z. Qu, T. Li, B. Wang, M.-f. Ye, X. Zhao, Y.-y. Yao, D.-S. Lü, and L. Liu, *Chinese Physics B* **27**, 073701 (2018).
- ¹¹J. L. Booth, P. Shen, R. V. Krems, and K. W. Madison, *New Journal of Physics* **21**, 102001 (2019).
- ¹²P. Shen, K. W. Madison, and J. L. Booth, *Metrologia* **57**, 025015 (2020).
- ¹³P. Shen, K. W. Madison, and J. L. Booth, *Metrologia* **58**, 022101 (2021).
- ¹⁴D. Barker, N. Klimov, E. Tiesinga, J. Fedchak, J. Scherschligt, and S. Eckel, *Measurement: Sensors* **18**, 100229 (2021).
- ¹⁵S.-Z. Zhang, W.-J. Sun, M. Dong, H.-B. Wu, R. Li, X.-J. Zhang, J.-Y. Zhang, and Y.-J. Cheng, *Acta Phys. Sin.* **71**, 094204 (2022).
- ¹⁶L. H. Ehinger, B. P. Acharya, D. S. Barker, J. A. Fedchak, J. Scherschligt, E. Tiesinga, and S. Eckel, *AVS Quantum Science* **4**, 034403 (2022).
- ¹⁷C. Makrides, D. S. Barker, J. A. Fedchak, J. Scherschligt, S. Eckel, and E. Tiesinga, *Physical Review A: Atomic, Molecular, and Optical Physics* **99**, 042704 (2019).
- ¹⁸C. Makrides, D. S. Barker, J. A. Fedchak, J. Scherschligt, S. Eckel, and E. Tiesinga, *Physical Review A: Atomic, Molecular, and Optical Physics* **101**, 012702 (2020).
- ¹⁹C. Makrides, D. S. Barker, J. A. Fedchak, J. Scherschligt, S. Eckel, and E. Tiesinga, *Physical Review A: Atomic, Molecular, and Optical Physics* **105**, 039903 (2022).
- ²⁰C. Makrides, D. S. Barker, J. A. Fedchak, J. Scherschligt, S. Eckel, and E. Tiesinga, *Physical Review A: Atomic, Molecular, and Optical Physics* **105**, 029902 (2022).
- ²¹J. Klos and E. Tiesinga, *The Journal of Chemical Physics* **158**, 014308 (2023).
- ²²D. S. Barker, J. A. Fedchak, J. Klos, J. Scherschligt, A. A. Sheikh, E. Tiesinga, and S. P. Eckel, *AVS Quantum Science* **5**, 035001 (2023).
- ²³S. Eckel *et al.*, in preparation (2023).
- ²⁴K. Madison, J. Booth, P. Shen, and R. Krems, Quantum pressure standard and methods for determining and using same (2018).
- ²⁵R. A. Stewart, P. Shen, J. L. Booth, and K. W. Madison, *Physical Review A: Atomic, Molecular, and Optical Physics* **106**, 052812 (2022).
- ²⁶P. Shen, E. Frieling, K. R. Herperger, D. Uhland, R. A. Stewart, A. Deshmukh, R. V. Krems, J. L. Booth, and K. W. Madison, *New Journal of Physics* (2023).
- ²⁷W. Bowden, W. Gunton, M. Semczuk, K. Dare, and K. W. Madison, *Review of Scientific Instruments* **87**, 10.1063/1.4945567 (2016).
- ²⁸W. J. Bowden, *An Experimental Apparatus for the Laser Cooling of Lithium and Rubidium*, Ph.D. thesis, University of British Columbia (2014).
- ²⁹K. Jousten, in *Handbook of Vacuum Technology* (John Wiley & Sons, Ltd, 2016) Chap. 11, pp. 463–510.
- ³⁰J. Jiang, J. Mitroy, Y. Cheng, and M. W. Bromley, *Atomic Data and Nuclear Data Tables* **101**, 158 (2015).
- ³¹B. A. Tom, S. Bhasker, Y. Miyamoto, T. Momose, and B. J. McCall, *Review of Scientific Instruments* **80**, 016108 (2009), https://pubs.aip.org/aip/rsi/article-pdf/doi/10.1063/1.3072881/14827893/016108_1_online.pdf.
- ³²A. Ridinger, S. Chaudhuri, T. Salez, U. Eismann, D. R. Fernandes, K. Magalhaes, D. Wilkowski, C. Salomon, and F. Chevy, *The European Physical Journal D* **65**, 223 (2011).
- ³³A. Burchianti, G. Valtolina, J. Seman, E. Pace, M. De Pas, M. Inguscio, M. Zaccanti, and G. Roati, *Physical Review A* **90**, 043408 (2014).
- ³⁴A. Deshmukh, A model of quantum diffractive heating, personal communication (2023), talk at the Quantum Sensors for Vacuum Metrology, Vancouver, Canada, May 12, 2023.
- ³⁵A. Deshmukh, R. A. Stewart, P. Shen, J. L. Booth, and K. W. Madison, Trapped particle evolution driven by residual gas collisions (2023), arXiv:2310.04583 [physics.atom-ph].
- ³⁶A. Derevianko, S. G. Porsev, and J. F. Babb, *Atomic Data and Nuclear Data Tables* **96**, 323 (2010).
- ³⁷M. S. Child, *Molecular Collision Theory* (Academic Press, London and New York, 1974).
- ³⁸A. A. Medvedev, V. V. Meshkov, A. V. Stolyarov, and M. C. Heaven, *Physical Chemistry Chemical Physics* **20**, 25974 (2018).